Surface deformation along the Carmel Fault System, Israel

Joerg Reinking, Hillrich Smit-Philipp, Gilad Even-Tzur

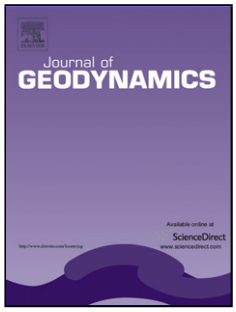

Title: Surface deformation along the Carmel Fault System, Israel

Authors: Joerg Reinking, Hillrich Smit-Philipp, Gilad Even-Tzur

PII: S0264-3707(11)00046-9
DOI: doi:10.1016/j.jog.2011.03.004
Reference: GEOD 1053

To appear in: *Journal of Geodynamics*

Received date: 19-11-2010
Revised date: 22-3-2011
Accepted date: 22-3-2011

Please cite this article as: Reinking, J., Smit-Philipp, H., Even-Tzur, G., Surface deformation along the Carmel Fault System, Israel, *Journal of Geodynamics* (2010), doi:10.1016/j.jog.2011.03.004

Surface deformation along the Carmel Fault System, Israel

Joerg Reinking[a], Hillrich Smit-Philipp[a], Gilad Even-Tzur[b]

[a]Department of Construction and Geoinformation, Jade University of Applied Sciences, Ofener Str. 16, 26121 Oldenburg, Germany (reinking@jade-hs.de, phone +49-441-7708-3250)

[b]Department of Civil and Environmental Engineering, Technion – Israel Institute of Technology, Technion City, Haifa 32000, Israel

Abstract

The existing knowledge about the recent crustal deformations along the Carmel Fault in Northern Israel which passes the city of Haifa is to a certain degree ambiguous. Depending on geological, geophysical or geodetic sources the movement rates and senses range from 1mm/yr sinistral up to 4 mm/yr dextral. In this paper we analyze GPS data from a regional network observed between 1999 and 2009 and derive global and regional velocities for 23 sites along the fault. The regional site velocities were estimated with respect to a local datum that was defined by a stable cluster of sites on one side of the fault and the horizontal velocity field shows deformations of up to 4.5 mm/yr dextral. In combination with an S-transformation the site velocities were used to estimate the parameters of a dislocation model based on elastic half space theory. We compare the results with expectations from slip rate analysis of seismicity parameters. In addition the resulting fault slip field is used to derive a fault-related velocity field.

Keywords: Carmel Fault; GPS; Velocity field; Dislocation model

1. Introduction

The Carmel Fault (CF) is the northwestern part of Carmel-Tirtza Fault System in Northern Israel and a generally northwestern branch of the Dead Sea Fault System (DSF) (Fig. 1). It is one of the major geological structures of northern Israel and comprises southern and northern NW-SE striking segments and a short central N-S striking segment in between. The fault crosses the city of Haifa and passes close to the petrochemical factories of the industrial area of Haifa Bay. Any damage to these factories, which are located in the vicinity of the city of Haifa, could cause a severe environmental disaster. Although this hazardous situation is well known the existing knowledge about recent crustal movements along the CF is to a certain degree ambiguous.

According to geophysical studies the surrounding area of the CF is a relatively high seismic active region (Hofstetter et. al., 1996). Geological studies (Zviely et. al., 2009) on sedimentary rocks show maximum vertical offsets of about 0.06 mm/yr in the last 600 thousand years. The horizontal velocities were estimated from displaced alluvial fans and stream channels to be of less than 1 mm/yr (Achmon, 1986) with a left-lateral sense. A sinistral sense of displacement also characterizes some of the earthquake epicentres detected along the CF (Hofstetter et. al., 1996). Recent geodetic results based on GPS observations in the same sites show controversial displacement rates and senses, ranging from 3.5 mm/yr dextral (Agmon, 2001), through 1 mm/yr sinistral (Ostrovsky, 2005) to about 4 mm/yr sinistral (Shahar and Even-Tzur, 2005). Latest investigations using PSInSAR (Nof et. al., 2007) did not show any evidence for differential surface displacement along the CF while a vertical slip of up to 1 mm/yr or horizontal slip of up to 4 mm/yr along the NW-SE segments of the CF cannot be totally rejected.

In this study we investigate GPS data from a regional network that has also been used by Agmon (2001), Even-Tzur (1991) and Ostrovsky (2005) and that was collected between 1999 and 2006. Data from a new GPS observation campaign in 2009 are additionally introduced. All data sets were re-calculated using the latest version of the Bernese GPS Software based on a common set of IGS (International GNSS Service) sites and additional regional permanent sites in conjunction with precise orbit and EOP (Earth Orientation Parameters) data. The analysis was done in consistency with the IGS05 reference frame, the GPS-only realization of the ITRF2005, whereby, in contrast to previous GPS analyses, absolute antenna phase centre offsets could be introduced. The use of permanent IGS

and regional sites gave the possibility for a quality check and, in addition, a comparison of the estimated velocity field with an ITRF2000-related velocity field presented by Wdowinski et al. (2004).

We defined a local datum according to Shahar and Even Tzur (2005) based on three sites on the west side of the CF. Since the accuracy of vertical position is low relative to horizontal position we only estimated the horizontal site velocities. The site velocities reach significant values of up to 4 mm/yr showing dextral movements along the fault. We introduced the site velocities into an elastic dislocation model with respect to the local geodetic datum definition, that we took into account by a simple similarity transformation (S-transformation), by which the coordinates of network sites can be transformed linearly to any desired datum. The resulting fault slip field can also be used to derive a fault-related velocity field.

2. Background and GPS network

According to Matmon et. al. (2003) the area under investigation can be divided into three distinct parts: Upper Galilee in the north, Lower Galilee in the centre and the Carmel region in the south (Fig. 2). According to the analysis of the seismic activity (Hofstetter et. al., 1996), the CF appears to be a boundary between two micro plates whereby the southern micro plate is stable while the northern micro plate shows deformations distributed in a wide range.

Matmon et. al. (2003) showed that the morphological and tectonic history of Galilee and their adjacent bounding blocks are best described by a set of two opposite facing halfgrabens. The southern halfgraben which is bounded in the south by the CF was formed during the Miocene, according to these authors, under a stress field related to the opening of the Red Sea and the Gulf of Suez. The western part of the CF is defined by a single fault. To the east, the CF splays into a series of E–W trending normal faults, which extend to the DSF valley. The activity along the CF predated the activity of the DSF and the adjacent Yizre'el Valley was formed associated with the opening of the Red Sea.

The Carmel region to the southwest of the CF is formed mainly by the mountain range of Mt. Carmel in the northwest and the Menashe Hills in the southeast. The Carmel block is supposed to be uplifted and tilted away from the Lower Galilee during the forming of the halfgrabens (Matmon et. al., 2003). Additionally Hofstetter et. al. (1996) consider that the CF as absorbs part of the deformation of the Dead Sea Fault.

Fault plane analysis of smaller earthquakes in this region show dominant left lateral strike slip along the north-western part of the CF and a complex tectonics on its south-eastern part. The last large earthquake in the area occurred 26 years ago (24/8/1984) with a magnitude of 5.3; the epicentre was 10km east of the CF. The last earthquake with a magnitude of at least 3.0 occurred in April 2010 very close to the fault middle segment. According to the seismic records, most seismic activity happened at a depth of ~10 to 25 km opposite to the fault middle segment (Hofstetter et. al., 1996).

The GPS network that was used to determine surface deformations consists of three parts that are combined in observation and analysis: the Carmel network, the G1 network and two sites of the Israeli network of permanent GPS sites APN (Active Permanent Network) (Fig. 3).

The Carmel network (Fig. 3, triangles) was established in 1990 and is composed of 17 points (Even-Tzur, 1991). The network was planned to monitor horizontal movements. In the planning stage the network was designed by assuming that three relatively rigid blocks exist in the area (Northern Carmel, Southern Carmel and Lower Galilee), which are in a state of lateral motion with respect to each other. Each block was marked by at least four points. The network points were marked, without an exception, on exposed and solid bedrock. Four points from the original network were destroyed during the years due to massive development in the region.

The G1 network (Even-Tzur, 2006) was designed and established by the Survey of Israel (SOI) and the Geological Survey of Israel (GSI) in the beginning of the 1990s with the intention of monitoring crustal deformation and serving as the major control network in Israel. The marks were built according to high technical specifications to ensure their geotechnical stability. The network consists of about 160 sites covering the major geological structure of Israel. Nine of the G1 sites (Fig. 3, circles) are combined with the Carmel network. Two of them are located close to two sites of the Carmel network giving the possibility to double-check resulting site velocities.

Additionally, data from seven sites of the Israeli network of permanent GPS sites APN (Wdowinski et. al., 2001) are included in the GPS analysis. Two of these sites (Fig. 3, squares) are in the vicinity of the network and therefore are incorporated in the deformation analysis. One of the sites (BSHM) is close to another Carmel network site.

3. GPS campaigns and data analysis

The first GPS observation campaigns in the Carmel network were carried out in the beginning of the 1990s by the Technion, Haifa. The early data sets suffer from a lack of dual-frequency data or short observation periods. The first campaign using dual-frequency receivers and spanning acceptable observation periods was carried out in 1996. Additional data from campaigns in 1999, 2002, 2006 and 2009 are available. Not all sites were occupied in all of the campaigns. Some of the campaigns were used also for additional purposes and therefore contain data of sites not included in the combined network described above.

To ensure a consistent datum definition for all campaigns additional data from APN sites and three supplementary IGS sites were used in the present GPS analysis. The non-permanent sites were occupied using tripods for the Carmel network point while the G1 network sites were measured using special centring devices, which allow an easier setup of the antenna. All sites were occupied at least twice with observation time spans of between 4 to 24 hours. The repeated occupation allows checking for the repeatability of site co-ordinates. The data for all sites of interest are listed in Tab. 1.

The GPS data analysis was done using the latest Bernese GPS Software Version 5.0 (Beutler et. al., 2007) with precise ephemeris and EOPs from IGS. Absolute phase centre variations with respect to IGS05 standard were used for all campaigns. To ensure the consistency of all campaign solutions we introduced the extrapolated IGS or SOPAC (Scripps Orbit and Permanent Array Center) co-ordinates for IGS stations and APN network sites as approximate co-ordinates. The datum was defined by loose constraints of the IGS and APN site co-ordinates. This allowed reducing the influence of possible seasonal variations of site co-ordinates which are not covered by linear IGS velocities.

As can be seen in Tab. 1 only a few permanent stations were available for the analysis of the 1996 campaign. Therefore, the definition of the datum is weak in comparison to the other campaigns. Additionally only some G1 network sites were observed. Consequently, we decided to exclude this campaign from the deformation analysis to avoid the influences of doubtful datum definition.

The data of the 2002 campaign also do not include a Carmel network site. The sites of the G1 network where measured over very large time span (> 1 year). Since seasonal site displacement cannot be precluded, a stable datum definition for the whole campaign is hard to identify. Also the comparison of the session solution cannot lead to a reliable quality check of the results. In addition, the definition of a reference epoch is not easy to deal with. Consequently we decided to exclude this campaign from the deformation analysis.

The repeatability of the remaining three campaigns (1999, 2006 and 2009) was checked by comparing the session solutions with the final combined campaign solution. Fig. 4 shows the average differences between final solutions and session solutions sorted for the different network components. The Carmel network component of the 1999 campaign shows larger differences particularly for the vertical component in contrast to the other three. This seems to be a result of short measurement sessions, not excludable multipath effects, centring problems of the GPS antenna or misreading of antenna heights. Therefore, the deformation analysis could not be based on height components. The results of the 2006 campaign make this decision apparent. Although the horizontal components for the G1 as for the Carmel network sites show acceptable average differences, the vertical component is not very reliable. The results of the 2009 campaign show -with rare exceptions- good results.

The comparison of the standard deviation of the site co-ordinates estimated by the Bernese GPS Software gives a similar picture, while the values are a bit greater than the average difference. This emphasises the overall acceptable quality of the resulting co-ordinates. However, the vertical component is not taken into account in any further analysis due to the irresolvable height problems of the early campaigns. The derived standard deviation can be used for weighting of the campaign solutions.

4. Global and regional site velocities

Three campaigns with acceptable horizontal co-ordinate quality over a period of ten years are obtained from the GPS analysis. The data are now used to derive site velocities by a least-squares adjustment process. Due to the fact that the time interval between the 1999 and 2006 campaign is about two times larger than that one between the 2006 and the 2009 campaign, the 1999 campaign would have a larger influence on the adjusted velocities. To reduce effects from the lower quality of this campaign data with respect to the other two campaigns we down-weighted the data from the 1999 campaign by a factor of 0.5 (following the time span relation) in relation to the other campaign data although analyses with equal weights do not show significant differences in the resulting site velocities.

The estimation of velocity vectors was carried out according to Even-Tzur (2004) as a two-step analysis with an adequate estimation of the variance factor. Full variance-covariance matrices from the GPS analysis were introduced to describe the correct stochastic model. Although the variance estimation from Bernese software seems to be too optimistic, we avoided introducing an often used and arbitrary selected scaling factor to the variance-covariance matrices of the GPS analysis. Using the two-step analysis, velocity residuals have a remarkable influence on the estimated standard deviation and therefore yield realistic error ellipses of the site velocities. We introduced an additional constraint for the velocities of adjacent sites (CR12-KRML, CR13-MRKA and CR10-BSHM) to ensure a consistent velocity adjustment.

At a first step we derived the velocities for the whole network described above excluding the three IGS sites using the original data from the GPS analysis. The resulting velocities are therefore defined in the global IGS05 datum. Fig. 5 shows the velocities and their 95% confidence ellipses (at the end of the vectors) for the northern part of the network which surrounds the CF. It can clearly be seen that the regional deformation field is superposed by global plate movements. The average velocity is about 3 cm/yr (Tab. 2) and reflects the movement of the Sinai sub-plate (Wdowinski et. al., 2004).

Wdowinski et. al. (2004) estimated the velocities of the APN network sites with respect to ITRF2000 taking into account the seasonal variations of the site co-ordinates. Table 2 shows the corresponding velocities of six sites derived from our analysis. The differences to the solution with Wdowinski et. al. (2004) are in the order of the amplitude of the seasonal co-ordinate variations. Taking into account additional effects resulting from discrepancies between IGS05 and ITRF2000 realisations, the results presented in this analysis could be seen to suit the global velocities well.

The IGS05-related velocity field does not clearly visualize the regional deformations. Hence, the derived velocity field must either be reduced by the superposing global velocities by means of an adjusted rotation with respect to an Euler pole or related to a set of regionally defined datum sites. The former was used by Wdowinski et. al. (2004) and this approach is initially used here too. We adjusted the position of the Euler pole and the angular velocity from the six sites of Table 2 and derived the values listed in Table 3 with their standard deviations.

Although the results fit well with those derived by Wdowinski et. al. (2004), it is clear that a reduction of the velocity field by the corresponding velocities would yield unreliable regional displacements due to the large standard deviation of the adjusted parameters. Also the values shown by Wdowinski et. al. (2004) cannot be used because they are related to ITRF2000 and not to IGS05. Therefore, we have to define a regional datum with respect to an undisturbed cluster of sites in the Carmel region. Such a cluster must not necessarily correlate with an identifiable geological “block” since it is only used to define a geometrical datum that can be introduced into the dislocation modelling later on.

Shahar and Even Tzur (2005) found a stable cluster of three G1 network sites (SFIA, MRKA and KRML) in the south-west of the CF which they used to define a “Carmel datum”.

We investigated the geometry of this cluster using the above presented results by means of statistical hypotheses tests. For this we transformed the campaign solutions of 1999 and 2006 into that of the 2009 campaign whereby the three sites of the cluster were introduced as “identical points”. The transformation was performed by an Euler rotation only to reduce the influence of the poorly defined vertical component on the one hand and to keep the scale of the IGS05 datum definition of the campaign solutions on the other hand. We found that with a significance of 95% the mentioned cluster

shows no significant deformation. Therefore, we use these three sites accordingly as a “Carmel datum” in the further analysis. This approach also keeps small but insignificant deformations of this cluster and does not constrain the relative velocities of the datum sites to zero.

After transforming the campaign solutions into the Carmel datum we calculated the velocity vectors using the approach that was also used for the global velocity field and applied once again the additional constraint for the velocities of adjacent sites. The resulting velocity field is shown in Fig. 6.

In the north-eastern part of the network the sites show significant horizontal velocities of up to 4.5 mm/yr. The sense of the displacement relative to the Carmel datum on the south-western side of the CF is dextral. All sites on the north-eastern side of the CF show the same sense of displacement.

The velocity field on the south-western side of the CF seems to be more complicated. In the southern part the sites CR16 and CR17 are displaced to the west-southwest direction while the northern part seems to have more north- to northeast-ward trend. In between there are some sites that show no significant or only very small velocities.

The derived velocity field cannot easily be explained; further, the datum definition is precise and clear but not very helpful for example for further tectonic analysis. However, additional modelling of the velocity field might lead to a better understanding on the deformation processes along the CF.

It should be mentioned that all sites used here are more than 30 km distant from the DSF. According to the investigations of Wdowinski et. al. (2004), at this distance the DSF should lead to similar velocities for all sites. Hence, we assume that relative velocities of the sites used here are only influenced by the movement along the CF.

5. Dislocation model

For the modelling of horizontal site velocities a number of possible approaches are available. They range from simple locked fault models (Even-Tzur, 2002; Savage and Burford, 1973) to viscoelastic finite elements models (FEM) (Suito et. al., 2002) and elastic half-space models (Klotz et. al., 2006; Okada, 1992). The first is much too simple for the complex setting at the CF. A FEM approach needs a good and detailed knowledge of the fault structure, which is only partially available for the CF. Therefore, we decided to use an elastic half-space approach which is simple enough to adjust for some unknown fault parameters and gives at least preliminary insights into the geodynamic behaviour of the study region.

We used the Green’s function of Okada (1992) for the strike slip and dip slip of a rectangular fault plane anddeveloped software that divides a complex fault into smaller patches and adjusts the strike slip and dip slip components of every patch using the horizontal velocity vectors as observation input. To smoothen the slips and avoid jumps of slips on adjacent patches we introduced the possibility of constraining the slip change between patches using a Laplacian operator according to Maerten et. al. (2005). To achieve more or less homogeneous slip values the magnitude of the constraint can be varied. A very tight constraint leads to similar slip values on all patches and as a limit all patches might have equal slips. In such a case all patches are seen as parts of a continuous fault plane.

The application of the Green’s function originally generates “absolute” dislocations from strike and dip slip defined in a fault-related datum whereas the measured and adjusted site velocities are defined in and therefore related to the Carmel datum. To consider the different definitions the Carmel datum was introduced into the least-squares adjustment of the fault plane slips by a simple similarity transformation (S-transformation). If we define the vector of fault-related site velocities as $\mathbf{u}_a$, the matrix of Green’s function as **G** and the vector of strike and dip slips for all patches as **s**, the original relation is described by

$$\mathbf{u}_a = \mathbf{G}\,\mathbf{s} \qquad (1)$$

The Carmel datum is defined by a similarity transformation matrix $\mathbf{H}_d$ in which except the rows related to the G1 network site SFIA, MRKA and KRML all values are set to zero and which is used as a condition matrix in the free adjustment of the site velocities. According to Wolf (1977) every solution of

the velocity vector $\mathbf{u}_i$ can be transformed into the defined datum by S-transformation using the condition matrix **H** of the free network adjustment (total trace minimization) by

$$\mathbf{u}_a = \mathbf{S}\mathbf{u}_i, \qquad (2)$$

while $\mathbf{S} = \mathbf{I} - \mathbf{H}(\mathbf{H}_d^T \mathbf{H})\mathbf{H}_d$.

Inserting (2) into (1) allows introducing a defined datum in the adjustment of strike slip and dip slip components:

$$\mathbf{u}_d = \mathbf{S}\mathbf{u}_a = \mathbf{S}\mathbf{G}\mathbf{s}. \qquad (3)$$

After fault slips are derived from a least squares adjustment the fault-related site velocities can be calculated simply from (1).

To model the CF we used basic fault system geometry where the position and length of the CF at surface was set-up according to Nof et. al. (2007) (Fig. 6). The depth of the top of the fault system was set to zero while the maximum depth of the system was set to 35 km (Fig. 7). The ends of the CF were extended to north-west and south-east to reduce unwanted effects at the edges. The whole fault system was separated into 5 segments (three segments in the middle that represent the CF part that is covered by the network and two extending segments) and split into 190 patches with approximately equal edge lengths of 3.5 km. The actual dip of the CF is not very well known. The focal plane solution of the 1984 earthquake (Hofstetter et. al., 1996) shows a dip of 60° to NE. Therefore we used fault planes with variable dip.

The dip of the fault system segments was varied in intervals of 15° between 60° to SW and 45° to NE for the northernmost segment and between 75° to SW and 45° to NE for the southernmost segment. The dip of the segments in between were adapted to the start and end segment so that a closed fault surface was formed. Fig. 7 shows the geometry of the fault system at the beginning of dip variation process.

The number of unknown strike slip and dip slip components of the least squares adjustment is twice the number of patches, hence 380, while the number of observed horizontal site velocities is twice the number of introduced sites, hence 46. Therefore it was mandatory to use constraints for the slip components. The strike slip components were constrained loosely. Due to the missing vertical data the dip slip components had to be constrained 100 times more strongly since small inhomogeneities of horizontal surface velocities would otherwise lead to unrealistic large dip slip components in the adjustment process.

The optimal dip of the segments was found in the variation process as a trade-off between the best fit of the modelled vectors to the observed vectors in terms of standard deviation and a homogeneous strike slip distribution on the fault plane. The most favourable result was attained with a dip of 75° to NE for the northernmost segment and a dip of 60° for the southernmost segment (Fig. 8).

The resulting strike slips are displayed in Fig. 9. Due to the orientation of the fault system from north to south negative values imply dextral movements while positive values represent sinistral deformation. The dip slip components are below 2 mm/yr and not presented here.

The resulting strike slip is still very inhomogeneous and shows large and unrealistic values of up to 25 cm/yr. Therefore we carried out an optimisation of the constraints for the strike slip component using the most favourable geometry of the fault system. The best result in terms of the mentioned trade-off shows that the constraints for the strike slip component should be increased by a factor of ten. The resulting strike slip distribution on the fault system planes is much more homogeneous and of the corresponding displacements are less than 25 mm/yr in extreme cases (Fig. 10), with an average of -2.8 mm/yr. The resulting dip slip field shows an average value of below 0.5 mm/yr and will therefore again be ignored.

Neglecting the northern and southern extending segments, the inner segments show dextral movements for the northern and southern parts of the fault system whereas the part than runs from north to south in its middle shows sinistral displacements (Fig. 11). One should keep in mind that Fig.

11 represents a flattened 2D plot of the 3D fault plane system. The maximum strike slip for the inner segments is 12 mm/yr with an average value of -0.55 mm/yr and a standard deviation 0f 0.4 mm/yr. Shapira and Hofstetter (2010) assume that the slip rate along the faults that are branches of the DSF is about 10-20 times slower than that of the DSF. For the northern part of the DSF the slip rate was calculated as 4.2 mm/yr from GPS observations (Wdowinski et. al., 2004). Therefore, our results seem to correspond with those of other investigations although this is not necessarily significant.

The observed and modelled site velocity vectors are presented in Fig. 12. The vectors in the north-west of the CF are not modelled correctly. It seems as if the dislocation of these sites cannot be explained by strike slip movements on the fault only. On the other hand, the introduction of lower constraints for dip slip components would impose a vertical displacement of the related sites due to the geometry of the fault which is not controlled by observations and can therefore yield unrealistic results. It is clear that we cannot solve this dilemma as long as no measured vertical displacements are introduced in the modelling.

After several tests we found that the fit could be improved if a second fault system is introduced which starts at the southern end of the middle segment, running in south-westward direction. Such a fault system has been considered by Bartov et. al. (2002) based on geological, geophysical, and geomorphological data. Fig. 13 shows the resulting site velocities. Although two vectors west of the CF remain poorly modelled, the fit for all other vectors is improved. The standard deviation was significantly reduced from 1.6 mm/yr for the best solution without this second fault system to 1.2 mm/yr for the solution including the second fault system.

By using equation (2) the Carmel datum can be removed from the modelled vectors and the resulting “absolute”, fault-related vectors were also computed. Fig. 14 shows the resulting gridded velocity field for the area of the CF. The region west of the middle segment seems to be driven by a rotational movement which is centred close to this segment. This area is permeated by numerous other faults that were investigated by Rotstein et. al. (2004). According to the results presented here, an extensional behaviour of this part of the area can be expected. This is in contrast to the assumption adopted by Rotstein et. al. (2004) and therefore needs to be investigated further in the future.

The derived strike slip and dip slip values allows the calculation of the strain rate according to Okada (1992). These were then used to calculate the second invariant strain rates, which are shown in Fig. 15 as colour-coded interpolated strain rate field. It can be clearly seen that the larger strain rates occur along the fault line. The largest strain rates are located close to the middle segment of the fault, which is close to the position of the last earthquake in April 2010.

6. Discussion and Outlook

The dislocation model presented here suffers from the lack of precise vertical information. Additionally, the complex geological structure of the Lower Galilee and adjacent regions is not considered in the model. Therefore, our model should be understood as preliminary and not as a reflector of reality. Nevertheless, some interesting aspects result from our analysis: it seems that west of the CF there are different deformation patterns in the north and in the south. Maybe this reflects the partition of Mt. Carmel and the Menashe Hills.

The analysis of GPS measurements over a period of ten years indicates a significant dextral movement along the CF during the last decade. This is in contrast to results from geological and geophysical surveys and must therefore be further investigated. Besides the campaign data sets used in this research two measurement campaigns from 1996 and 2002 of the G1 network will be recalculated and introduced in the deformation analysis. Furthermore, two additional campaigns of the whole network will be carried out by the authors in the next years with the aim of verifying the presented horizontal site velocities and possible accelerations.

In addition, the quality of the vertical displacements must be improved. Future campaigns will therefore be carried out with longer measurement sessions. It is also planned to combine data from precise levelling (Even-Tzur and Agmon, 2005) and from PSInSAR with the results of the GPS campaigns to enhance the information content of the vertical data. Altogether, this will allow reducing the tight constraints for the dip slip components in the elastic half-space model and, in so doing, deriving more reliable dip slip values as well

.

References

Achmon, M., 1986. The Carmel border fault between Yoqneam and Nesher. M.Sc thesis, Hebrew University of Jerusalem, Jerusalem (in Hebrew, with English abstract).

Agmon, E., 2001. Algorithm for the analysis of deformation monitoring networks. M.Sc. Thesis, Technion, Israel Institute of Technology, Haifa (in Hebrew, with English abstract)

Bartov, Y., Sneh, A., Fleischer, L., Arad, V., Rosensaft, M., 2002. Potentially active faults in Israel. Geol. Surv. Isr. Rep. GSI/29/2002.

Beutler, G., Bock, H., Dach, R., Fridez, P., Gäde, A., Hugentobler, U., Jäggi, A., Meindl, M., Mervart, M., Prange, L., Schaer, S., Springer, T., Urschl, S., Walser, P., 2007. Bernese GPS Software Version 5.0. Astronomical Institute, University Bern, http://www.bernese.unibe.ch/docs/DOCU50.pdf

Even-Tzur, G., 1991. Monitoring Deformation in the Carmel Mountain Region by GPS. M.Sc.Thesis, Technion, Israel Institute of Technology, Israel (in Hebrew).

Even-Tzur, G., 2002. GPS Vector Configuration Design for Monitoring Deformation Networks. Journal of Geodesy, 76(8), 455-461.

Even-Tzur, G., 2004. Variance Factor Estimation for Two-Step Analysis of Deformation Networks. Journal of Surveying Engineering, 130(3), 113-118.

Even-Tzur, G., Agmon, E., 2005. Monitoring Vertical Movements in Mount Carmel by Means of GPS and Precise Levelling. Survey Review, 38 (296), 146-157.

Even-Tzur, G., 2006. Designing the Configuration of the Geodetic-Geodynamic Network in Israel. Geodetic Deformation Monitoring: From Geophysical to Engineering Roles, Eds. Sanso, F., Gil, A., J. International Association of Geodesy Symposia, Springer, 131, 146-151.

Hall, J.K., 1996. Topography and bathymetry of the Dead Sea depression. Tectonophysics 266, 177–185.

Hofstetter, A., van Eck, T., Shapira, A., 1996. Seismic activity along fault branches of the Dead Sea-Jordan Transform System: The Carmel-Tirtza fault system. Tectonophysics 267, 317-330

Klotz, J., Abolghasem, A., Khazaradze, G., Heinze, B., Vietor, T., Hackney, R., Bataille, K., Maturana, R., Viramonte, J., Perdomo, R., 2006. Long-term signals in the present-day deformation field of the Central and Southern Andes and constraints on the viscosity of the Earth's upper mantle. In: Oncken, O., Chong, G., Franz, G., Giese, P., Götze, H.-J., Ramos, V.A., Strecker, M.R., Wigger, P. (Eds.) The Andes – active subduction orogeny. Frontiers in Earth Science Series, Vol 1. Springer-Verlag, Berlin Heidelberg New York, 65–90.

Maerten, F., Resor, P., Pollard, D., Maerten, L., 2005. Inverting for slip on three-dimensional fault surfaces using angular dislocations. Bull. Seismol. Soc. Am. 95, 654–665.

Matmon, A., Wdowinski, S., Hall, J.K., 2003. Morphological and structural relations in the Galilee extensional domain, northern Israel. Tectonophysics 371, 223-241

Nof, R.N., Baer, G., Eyal, Y., Novali, F., 2007. Recent Crustal Movements Along the Carmel Fault System, Israel. Proc. 'Envisat Symposium 2007', Montreux, Switzerland 23–27 April 2007 (ESA SP-636, July 2007)

Okada, Y., 1992. Internal deformation due to shear and tensile faults in a half-space. Bull.Seism.Soc.Am. 82, 1018-1040.

Ostrovsky, E., 2005. The G1 geodetic geodynamic network: results of the G1 GPS surveying campaigns in 1996/1997 and 2001/2002. Tech. Proj. Rep., Survey of Israel.

Savage, J.C., Burford, R.O., 1973. Geodetic determination of relative plate motion in central California. J. Geophys. Res. 78, 832– 845.

Shahar, L., Even Tzur, G., 2005. Deformation Monitoring in the Northern Israel between the Years 1996 and 2002. Geodetic Deformation Monitoring: From Geophysical to Engineering Roles, Eds. Sanso, F., Gil, A., J. International Association of Geodesy Symposia, Springer, 131, 146-151.

Suito, H., Iizuka, M., Hirahara, K., 2002. 3-D Viscoelastic FEM Modelling of Crustal Deformation in Northeast Japan. Pure appl. Geophys. 159, 2239-2259.

Shapira, A., Hofstetter, A., 2010. Seismicity Parameters of Seismogenic Zones, http://www.seis.mni.gov.il/heb/Teken/seismicity-rprt.htm

Rotstein, Y., Shaliv, G., Rybakov, M., 2004. Active tectonics of the Yizre'el valley, Israel, using high-resolution seismic reflection data. Tectonophysics 382, 31-50.

Wdowinski, S., Bock, Y., Forrai, Y., Melzer, Y., Baer, G., 2001. The GIL network of continuous GPS monitoring in Israel for geodetic and geophysical applications. Isr. J. Earth Sci. 50, 39–47

Wdowinski, S., Bock, Y., Baer, G., Prawirodirdjo, L., Bechor, N., Naaman, S., Knafo, R., Forrai, Y., Melzer, Y., 2004. GPS Measurements of Current Crustal Movements along the Dead Sea Fault. J. Geophys. Res., 109, 1-16.

Wolf, H., 1977. Eindeutige und Mehrdeutige Geodätische Netze. Abh. D. Braunschw. Wiss. Gesellsch, Band 28, Gottingen, Germany.

Zviely, D., Galili, E. Ronen, A., Salamon, A., Ben-Avraham, Z., 2009. Reevaluating the tectonic uplift of western Mount Carmel, Israel, since the Middle Pleistocene. Quaternary Research 71 (2), 239-245.

Figures

Fig. 1: Schematic plot Carmel Fault (CF, according to Bartov et. al. (2004)) in the context of Dead Sea Fault (DSF) and the eastern Mediterranean plate boundaries (NAF North Anatolian Fault, EAF East Anatolian Fault). Grey dashed line: not know extension of CF. DTM data according to Hall (1996).

Fig. 2: General location map of morphological and structural relations in the Galilee (Matmon et. al. 2003).

Fig. 3: Carmel Fault and GPS sites used in this analysis. Triangles: Carmel network, circles: G1 network, squares: APN network.

Fig. 4: Repeatability check by means of average differences between final solutions and session solutions.

Fig. 5: Velocity vectors and their 95% confidence ellipses related to IGS05.

Fig. 6: Velocity vectors and their 95% confidence ellipses related to the Carmel datum (sites SFIA, MRKA and KRML)

Fig. 7: Geometry of the fault system at the start of dip variation with a dip of 60° to SW for the most northern segment and 75° SW for the most southern segment. View from SW to NE.

Fig. 8: Geometry of the fault system for the most favourable result with a dip of 75° to NE for the most northern segment and 60° to NE for the most southern segment. View from NW to SE.

Fig. 9: Schematic perspective 3D-plot of strike slip distribution on the fault plane surface. Positive: sinistral, negative: dextral. Gray dots: middle point of patches with connecting lines.

Fig. 10: Schematic perspective 3D-plot of strike slip distribution on the fault plane surface using stronger constraints for strike slips. Positive: sinistral, negative: dextral. Gray dots: middle point of patches with connecting lines.

Fig. 11: Slip vectors (strike and dip slip) of the inner segments of the fault system. Northern and southern extensions are neglected. Vectors orientation: left: dextral, right: sinistral.

Fig. 12: Modelled velocity vectors using stronger constraints for strike slip.

Fig. 13: Modelled velocity vectors using a second fault system leads to a better fit for almost all vectors.

Fig. 14: Modelled vectors related to an “absolute” (fault related) datum.

Fig. 15: Second invariant strain rate along the CF.

Tables

Tab. 1: Available GPS data for all used campaigns

Tab. 2: IGS05 velocities and standard deviation in mm/yr. Differences (Δ_N, Δ_E) to ITRF2000 solution of (Wdowinski et. al. 2004).

Tab. 3: Adjusted Euler pole position (longitude λ, latitude φ), angular velocity (ω) and corresponding standard deviation (s_λ, s_φ, s_ω).

> We observed and analysed recent crustal movements along the Carmel Fault, Israel, by means of GPS.

> We found a dextral displacement along the fault of up to 4.5 mm/yr with respect to a regional datum.

> Inversion of the GPS-derived velocity field parameters and slip values at the fault are comparable with that one from other investigations.

> Derived strain rates show maxima close to the position of the last earthquake in April 2010.

	campaign					network
Site	1996	1999	2002	2006	2009	
CR02		●		●	●	Carmel
CR04		●				
CR05		●		●	●	
CR07		●		●	●	
CR09		●		●	●	
CR10		●		●	●	
CR11		●				
CR12		●		●	●	
CR13		●		●	●	
CR14		●		●	●	
CR15		●		●	●	
CR16		●		●	●	
CR17		●		●	●	
ATLT	●		●	●	●	G1
GLON	●	●	●	●	●	
KBIA			●	●	●	
KRML	●	●	●	●	●	
KRMV			●	●	●	
KRTV	●	●	●	●	●	
MRKA	●	●	●	●	●	
PARK			●	●	●	
SFIA	●	●	●	●	●	
ZPRI	●		●	●	●	
BSHM		●	●		●	APN
ELAT		●	●	●	●	
GILB		●	●	●	●	
KABR		●	●	●	●	
KATZ	●	●	●	●	●	
RAMO		●	●	●	●	
TELA	●	●	●	●	●	
ANKR	●	●	●	●	●	IGS
NICO		●	●		●	
ZECK		●	●	●	●	

λ	0.81 deg	s_λ	16.51 deg
φ	50.93 deg	s_φ	4.53 deg
ω	0.5186 deg/Myr	s_ω	0.1684 deg/Myr

Site	North mm/yr	σ_N mm/yr	East mm/yr	σ_E mm/yr	Δ_N mm/yr	Δ_E mm/yr
BSHM	20.49	0.08	22.54	0.16	-2.05	-0.43
GILB	20.99	0.06	21.59	0.13	-1.60	0.77
KABR	19.85	0.07	21.38	0.14	-0.98	0.64
KATZ	22.49	0.09	21.38	0.16	-1.19	0.85
RAMO	19.24	0.07	22.83	0.13	-1.24	0.01
TELA	19.92	0.07	21.90	0.14	-1.38	1.52

Figure1_color rev1

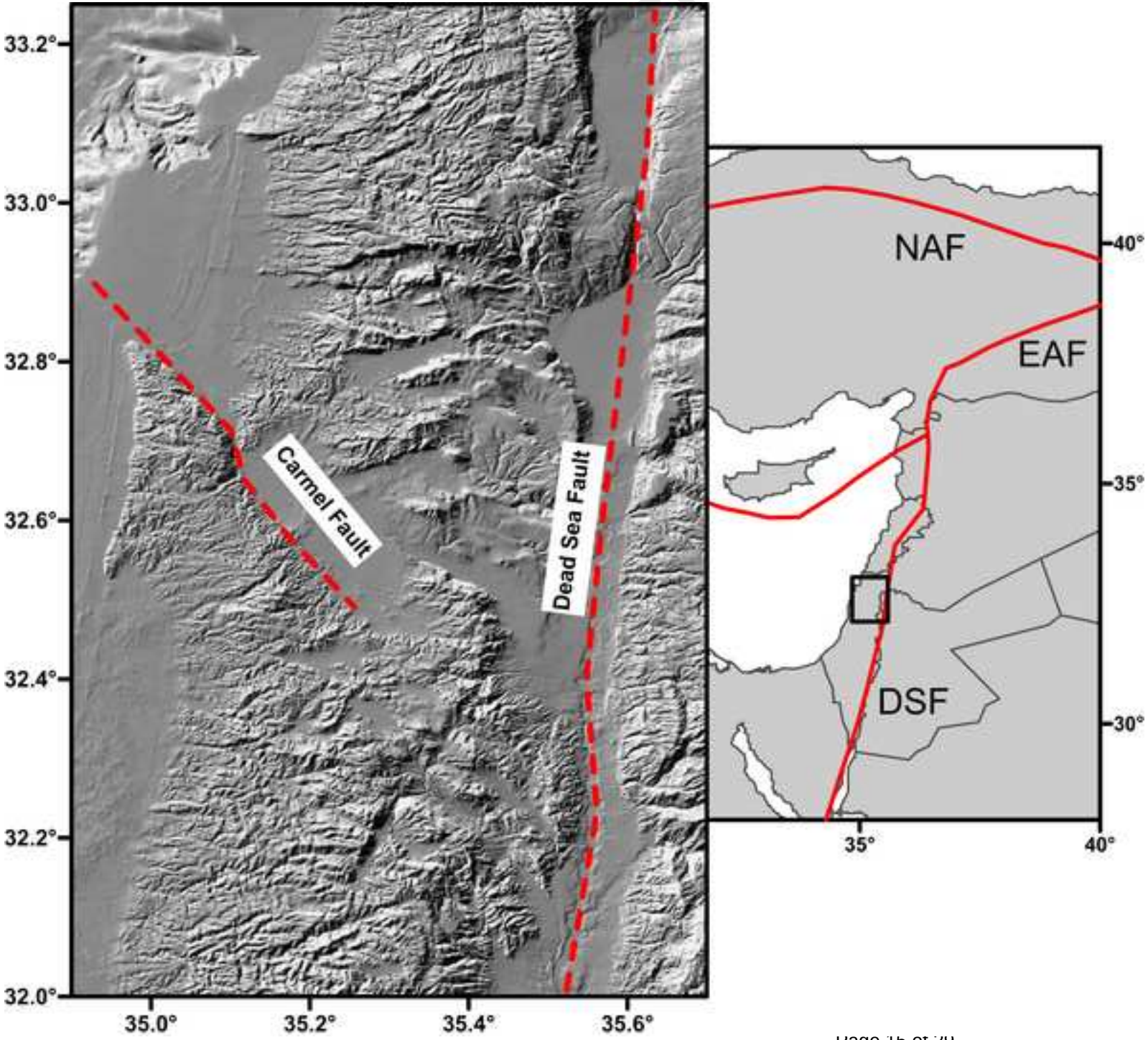

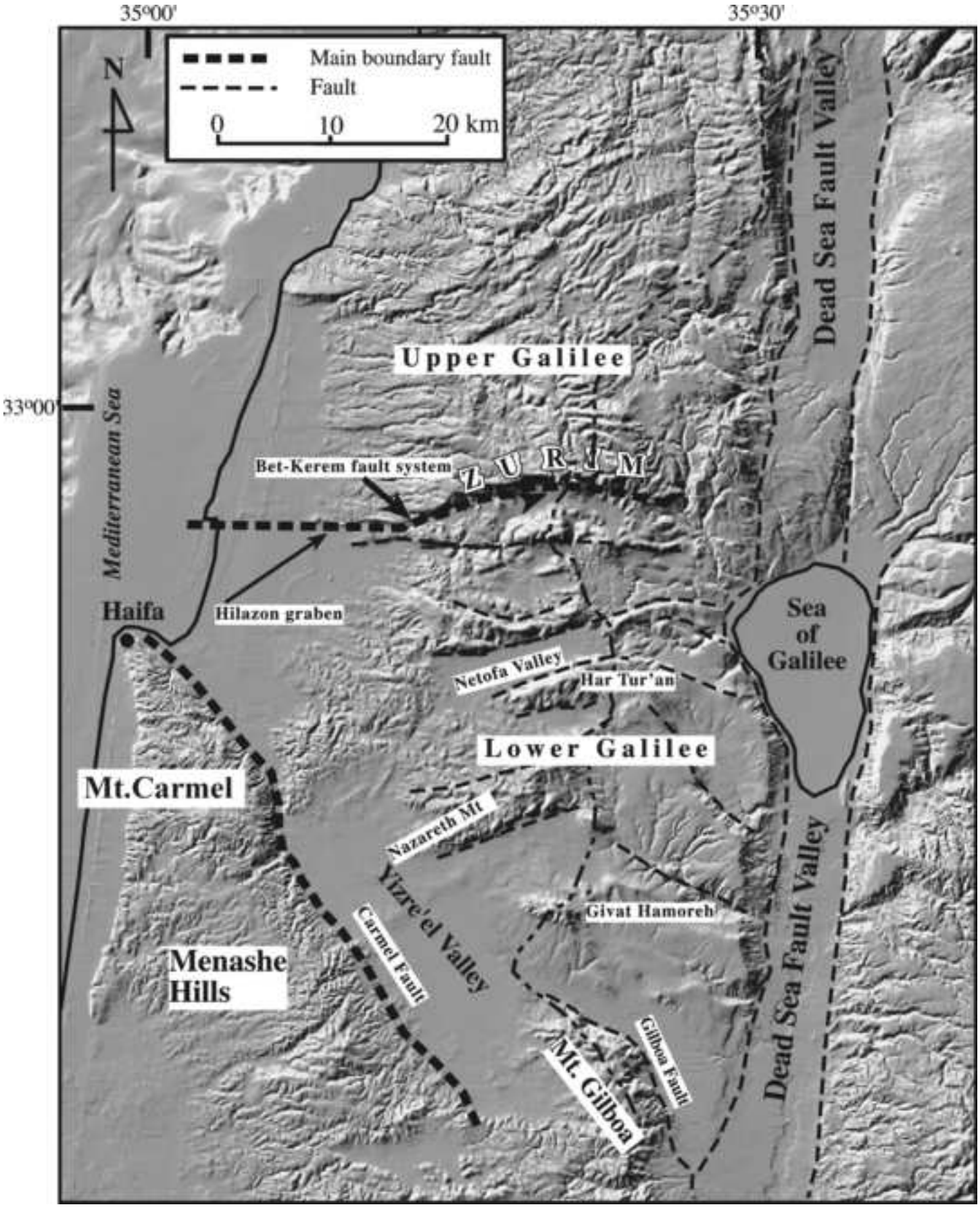

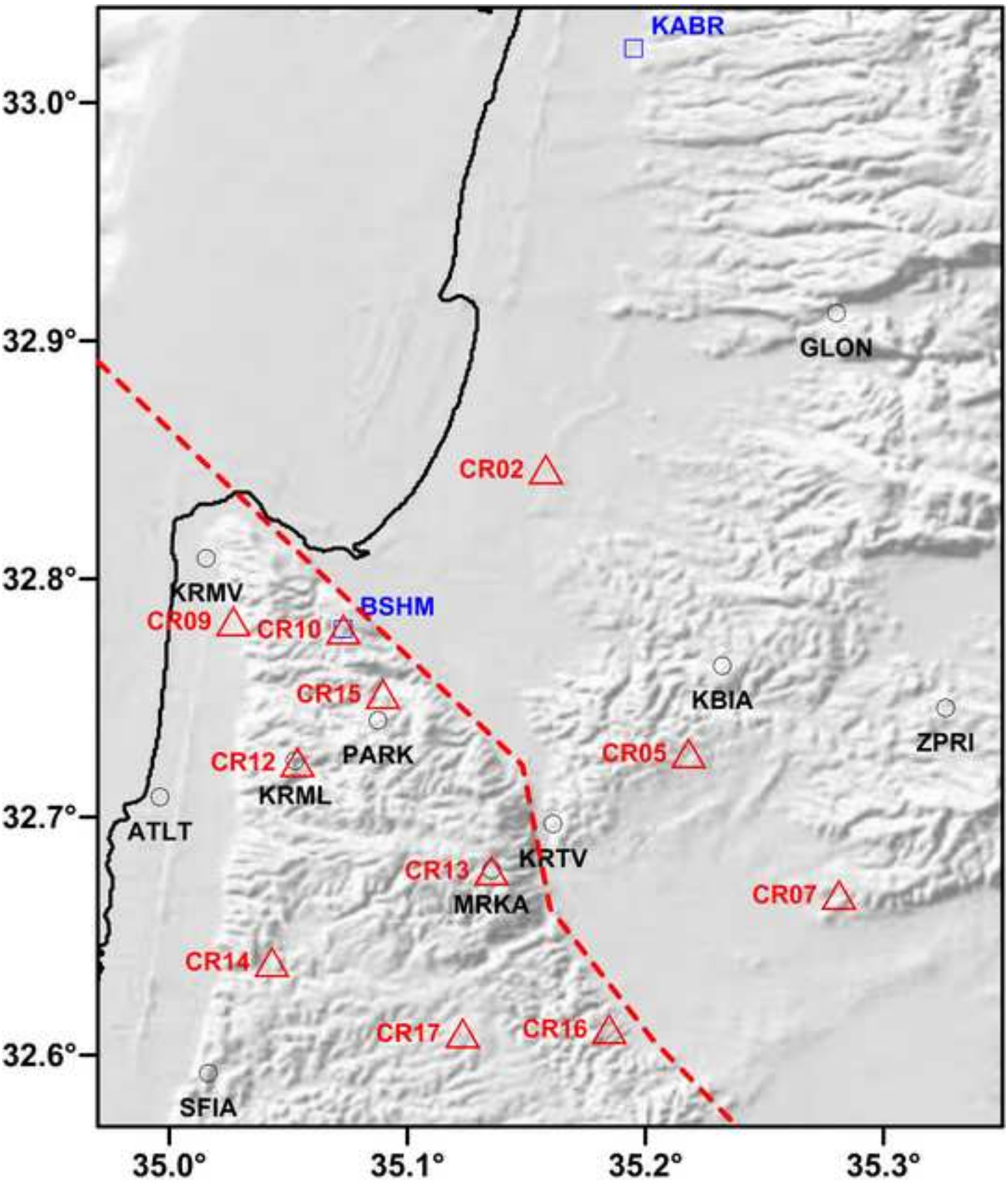

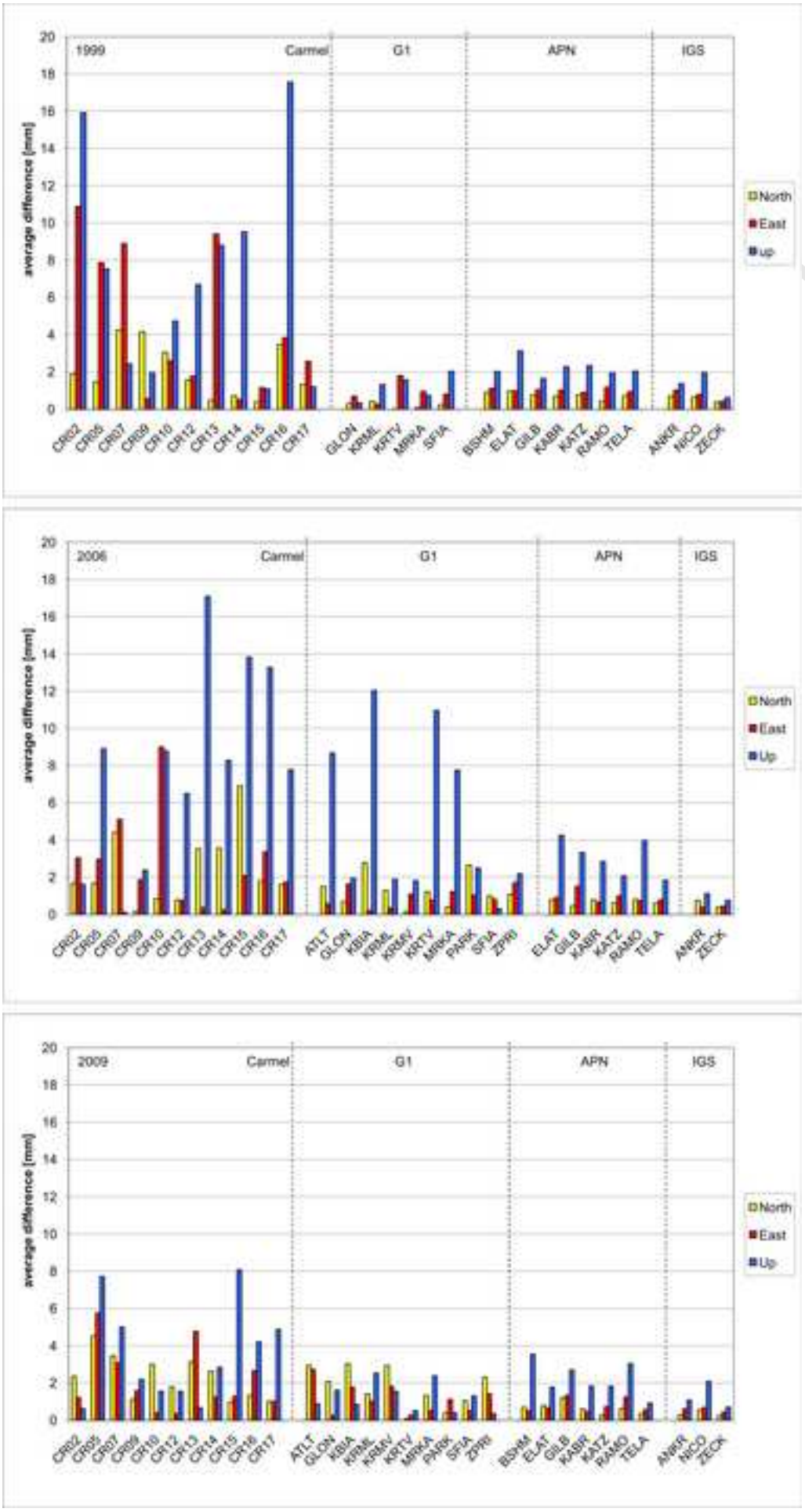

Figure5_color rev1

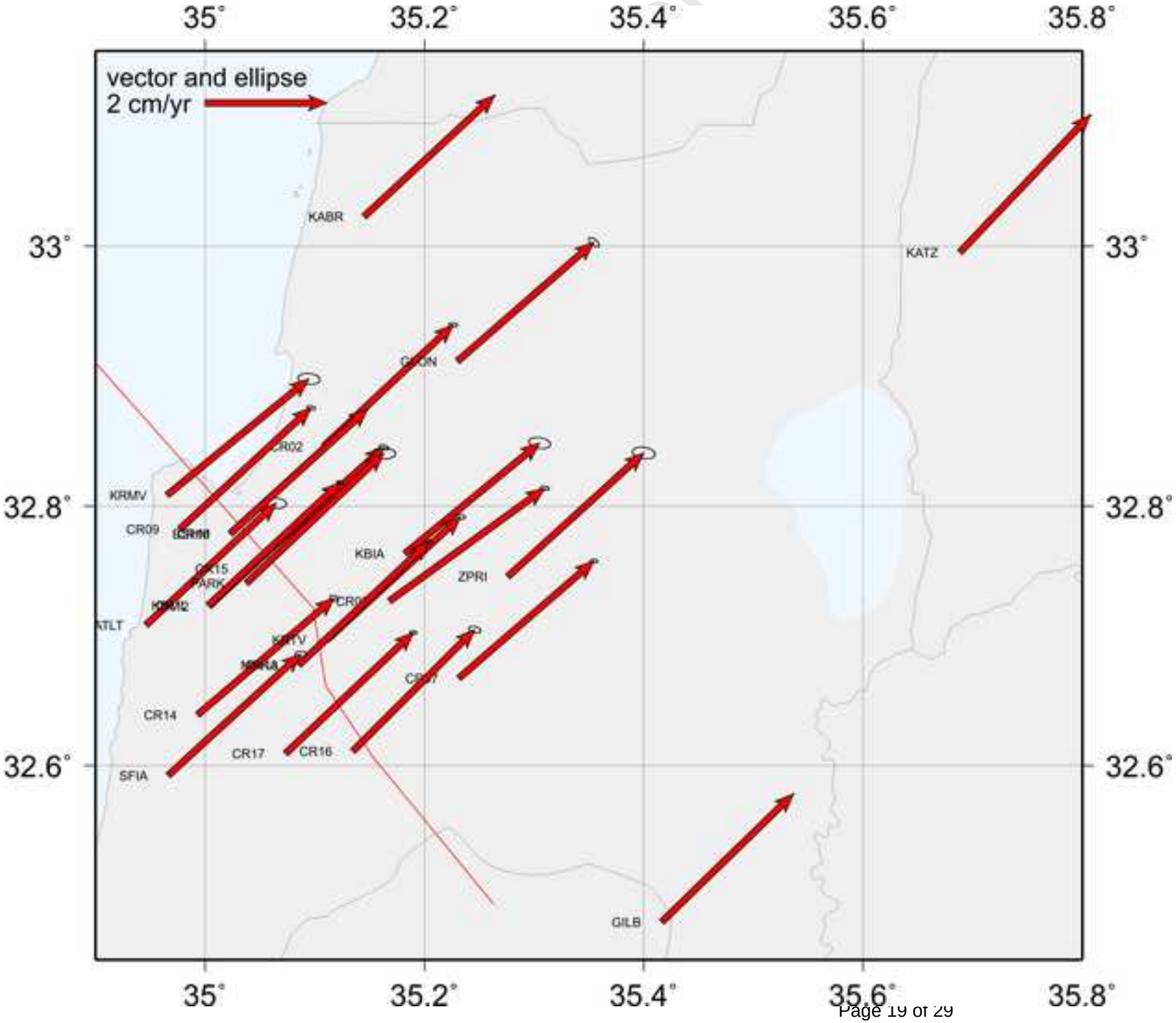

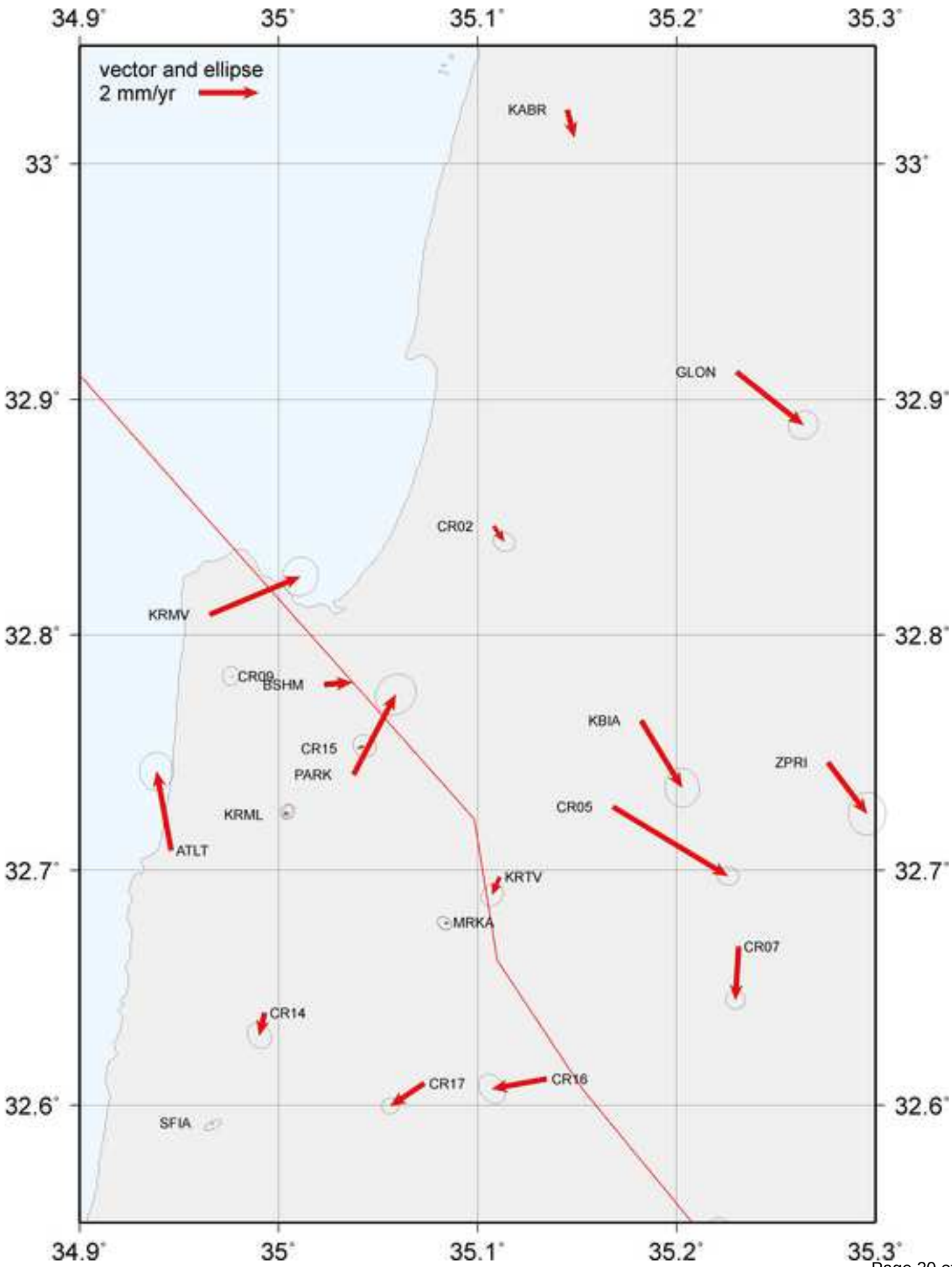

Figure7_color rev1

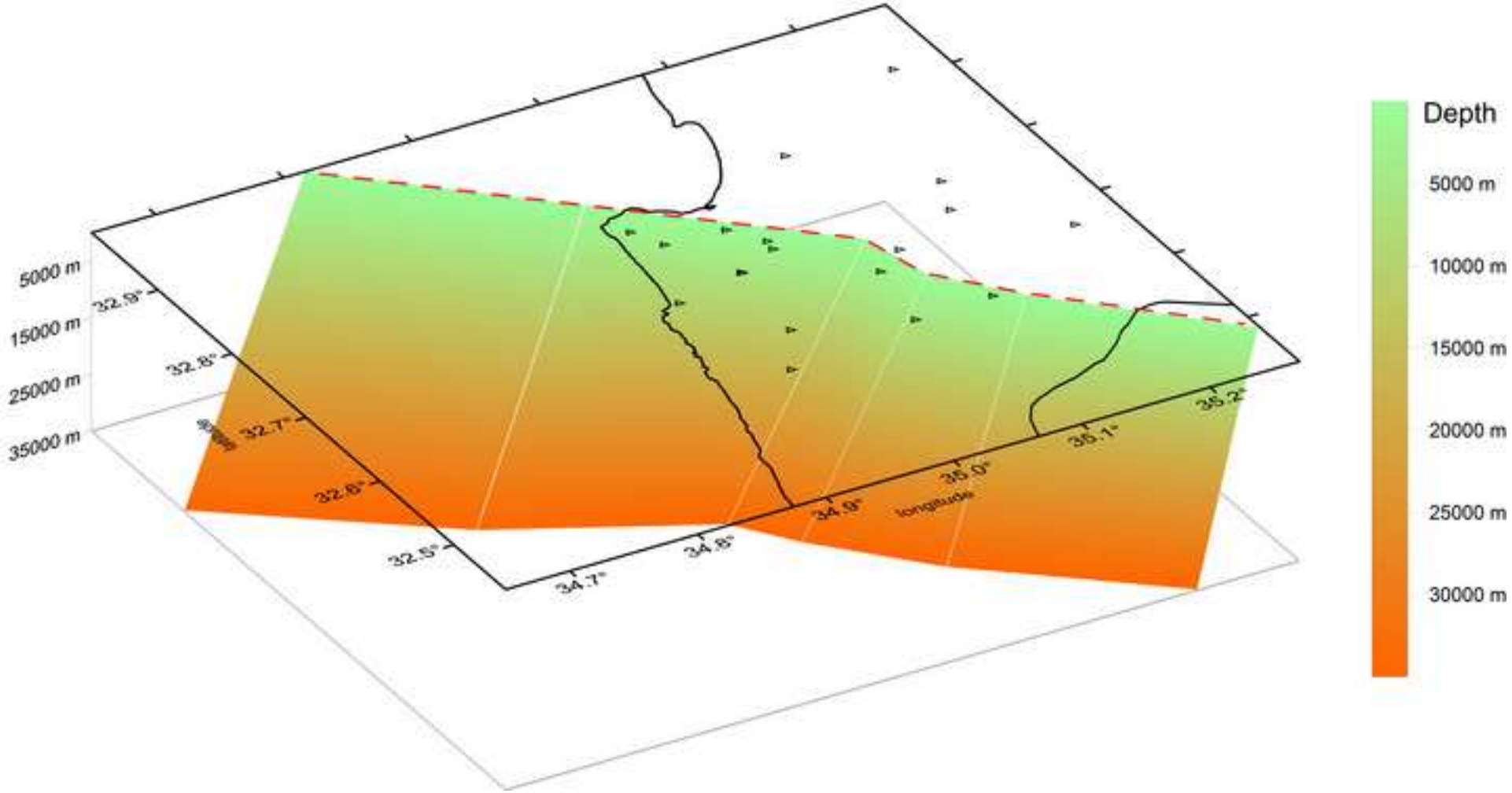

Figure8_color rev1

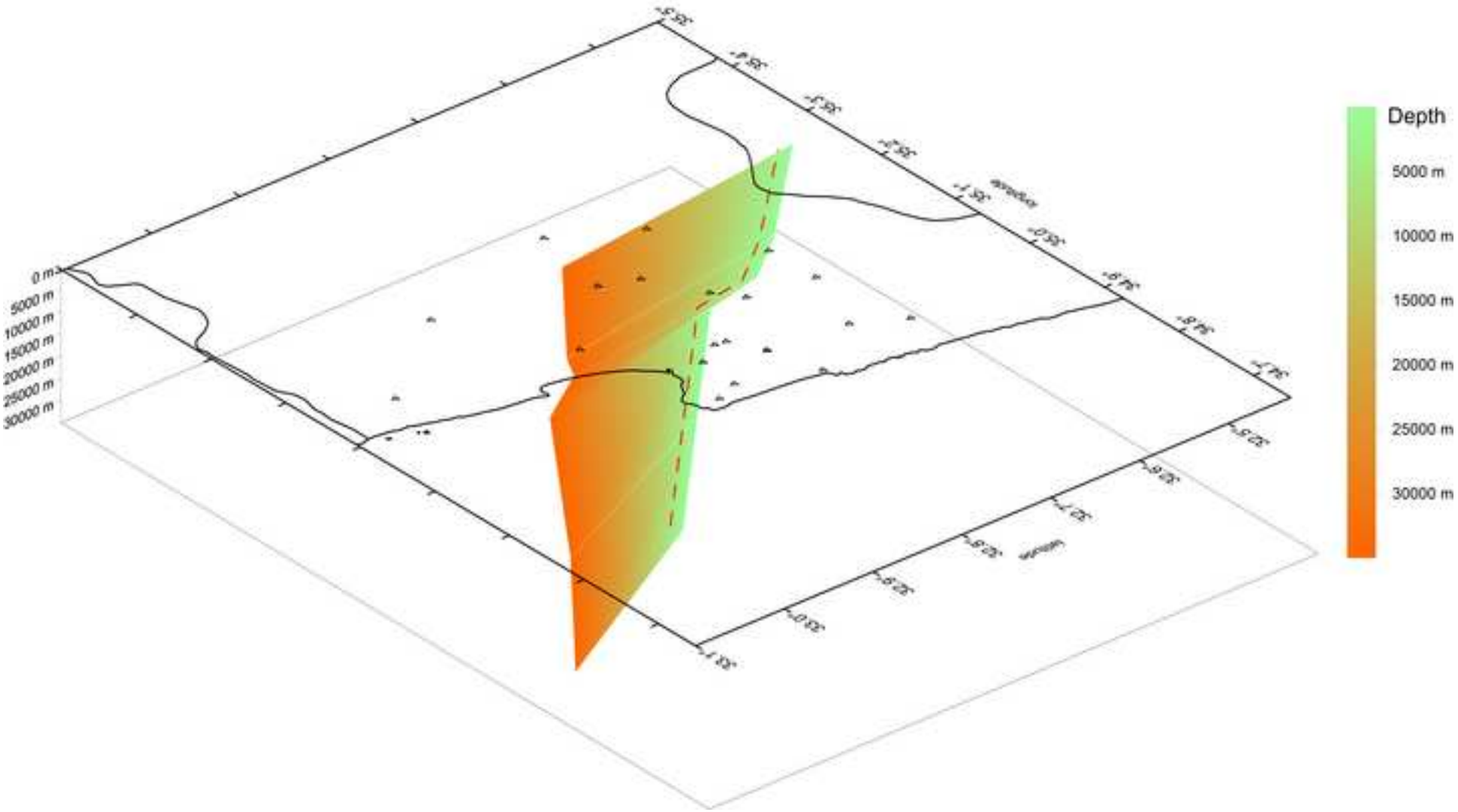

Figure9_color rev1

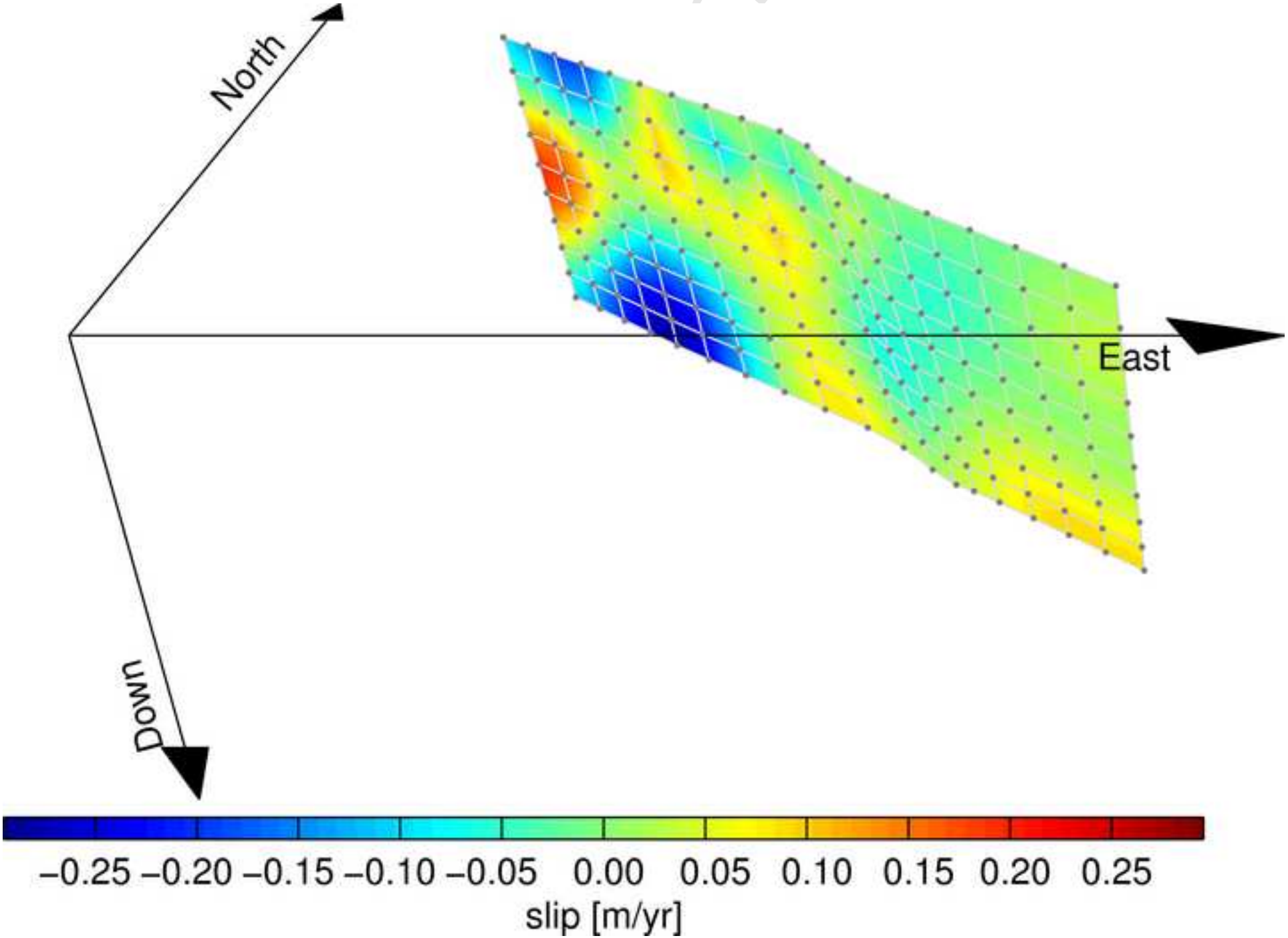

Figure10_color rev1

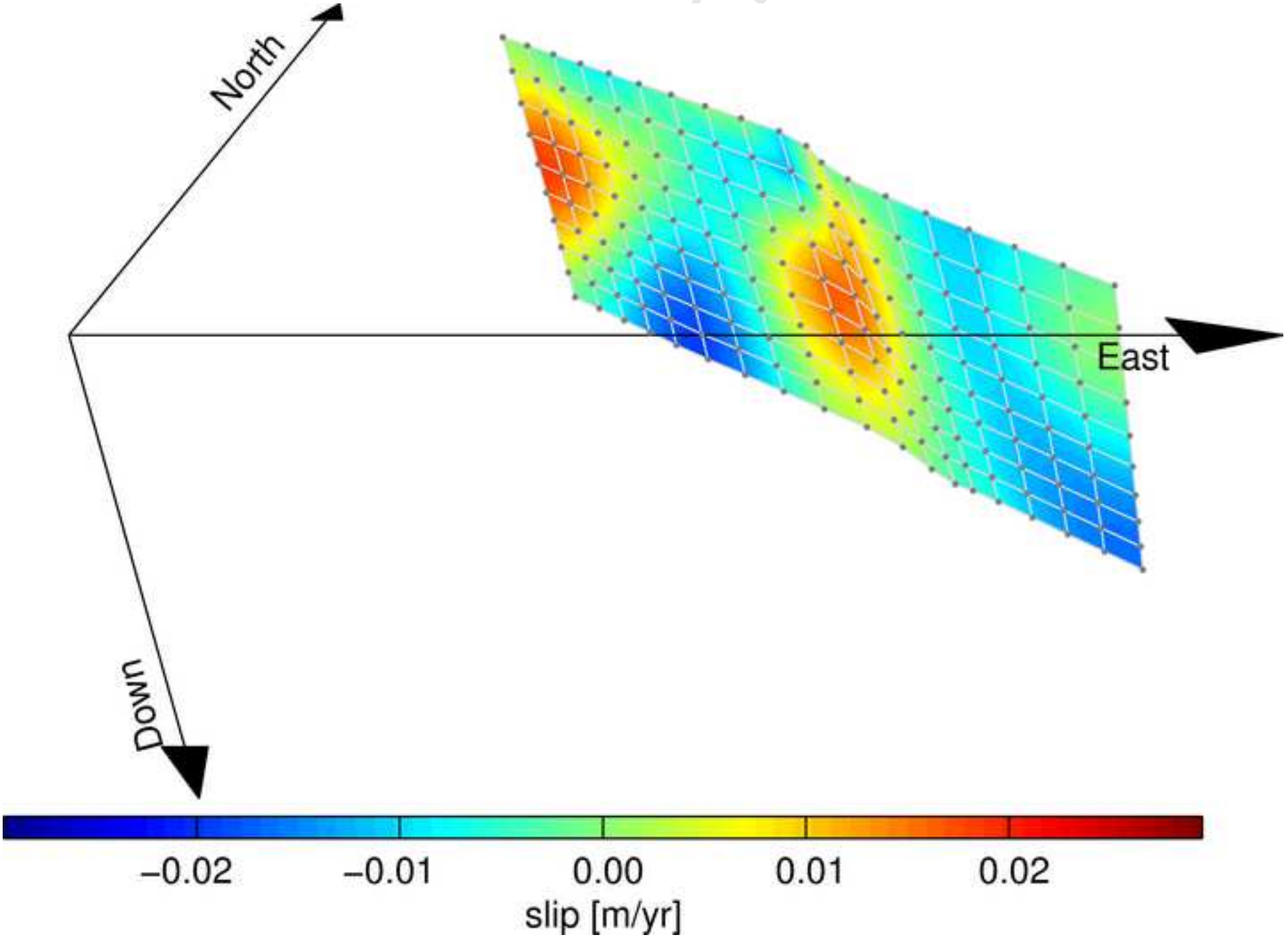

Figure11_color rev1